Academia Journal of Scientific Research 6(11): 000-000, November 2018
DOI: 10.15413/ajsr.2018.0221
ISSN 2315-7712

Academia Publishing

Research Paper

Failure mechanism investigation of bottom plate in concrete box girder bridges

Da Wang[1]*, Yongming Liu[2] and Yang Liu[1]

[1]School of Civil Engineering and Architecture, Changsha University of Science & Technology,960 2nd Section, Wanjiali South RD, Changsha, Hunan, P.R. China.
[2]School for Engineering of Matter, Transport and Energy, Arizona State Univ., 501 E. Tyler Mall， AZ 85281, USA.

*Corresponding author. E-mail: yxwang2006@sohu.com. Tel: +86-15874991489. Fax: +86-731-85256006.

Accepted 29th November, 2018

ABSTRACT

In the proposed study, the Linguo continuous rigid frame bridge was studied to determine the failure mechanisms by combining both field investigation and a 3D finite element (FE) method. The characteristics of the failure on the bottom plate were analysed and three typical failure models were identified. The failure mechanism was investigated and verified using a proposed 3D nonlinear FE model. Retrofit methods were proposed and implemented for the damaged bridges. The measured stress response and calculated stress response from the proposed 3D finite element model were compared. Satisfactory results were observed between field measurements and numerical simulations. Parametric studies were performed using the developed model to investigate several important parameters for the bridge design and construction. Finally, conclusions and recommendations for future bridge analysis and design were provided on the basis of the proposed study.

Key words: Failure mechanism, prestressed, crack, finite element, concrete box girder.

INTRODUCTION

Prestressed concrete box girder bridges are widely used because of their excellent properties, such as low cost and aesthetic appearance (Barr et al., 2005; Moon et al., 2005; Pan et al., 2010; Jung et al., 2010). A parabolic or circular curve gradient, similar to arranged prestressed strands, is usually adopted for the height of the cross section of this type of bridge to optimise the structural size and cantilever construction (Malm and Sundquist, 2010; Xiang et al., 2010). Radial force is generated by the curved prestressed strands and this type of force has been found to be responsible for the failure of the bottom plate (Xu et al., 2007; Peng, 2008). Furthermore, increased number of prestressed strands makes the space very busy within the bottom plate and aggregates the failure process due to the concrete filling. The failure of the bottom plate may lead to significant reduction in stiffness and strength, as well as loss of bearing capacity and collapse (El-Ariss, 2007; Bazant et al., 2008).

Vertical tension stress or transverse stress of the bottom flange is believed to be the most fundamental reason for failure (Podolny, 1985; Wei et al., 2007). Detailed quantitative studies for the influence of these factors are seldom reported. The failure mechanism under radial force remains controversial (Xiang et al., 2010) according to many existing studies. Pan et al. (2008) performed a field investigation and divided these cracks into two main groups, namely, longitudinal cracking and delamination of the flange base. Peng (2008) extended spalling as the third type of cracking. Xiang et al. (2010) presented four types of cracking of the bottom plate. Precise analysis of the structural system response of precast segment box girder bridges is required for the loading change that occurs during the construction sequence (Megally et al., 2002). The structural performance in the spatial thin-walled box structure is very complex and several 2D plane analysis have been used for structural design (Liao, 2004; Sennah and Kennedy, 2001; Ataei and Padgett, 2013). According to applicable codes (AASHTO, 2007; JTG D62-2004), the transverse effects are neglected because the influence of the arranged prestressed strands is mainly on the bottom

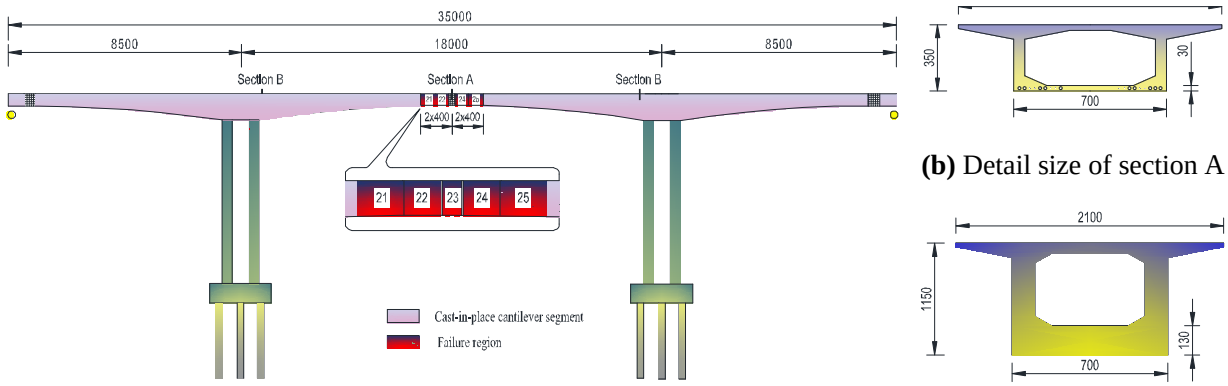

(a) Spans of Linguo Bridge

(b) Detail size of section A

(c) Detail size of section B

Figure 1: Layout of Linguo Bridge (Units: cm).

plate. For the box girder bridge, a wider box girder will have larger spatial effect and 3D finite element is preferred for more accurate local stress analysis.

Theoretical simulation of failure of the bottom plate during prestressing is difficult. The accurate and efficient modelling of the prestressed effect, as well as the analysis of the nonlinear process of failure is desired (Bergan and Holand, 1979; Orta and Bartlett, 2015). Previous studies have shown that the finite element (FE) method can be used for concrete box girders (El-Ariss, 2007; Sousa et al., 2013; Wu and Gilbert, 2009; Zhou, 2010; Lou et al., 2014). Some difficulties are involved in modelling of spatial prestressed action, which is rarely reported (Xiang et al., 2010). Prestressed strands should be individually modelled by FEs to analyse the details of the spatial prestressed action. Such individual modelling of prestressed strands and concrete is not compatible with the common framework in modelling of concrete and prestressed strands for the analysis of prestressed concrete structures. A very fine mesh has to be used for the concrete and prestressed strands elements, and a very large number of elements would be required. In addition, majority of the current studies are performed in the elastic range and the nonlinear material properties has not been considered (Guo et al., 2005; Pedziwiatr, 2009; Pimentel and Figueiras, 2015; Chen and Tang, 2015). The bottom plate of the box girder bridge enters the plastic stage before failure occurs. Bathe et al. (1989), proposed a nonlinear FE analysis of concrete structures, which was successfully applied by Xiang et al. (2010) and Tang et al. (2005). The similar methodology will be used in the proposed study.

The field observations of the bottom plate failure are discussed first and three major type of failure mechanisms are discussed. A 3D FE model with ANSYS program is proposed for a prestressed concrete continuous rigid frame bridge to explore the failure mechanism of the box girder bridge bottom plate. Prestressing was simulated, and the morphology and mechanism of failure were explored. A reinforcement method is proposed for the failure of the bottom plate. The effect of reinforcement was tested and verified with the collected testing data. The effects of the index of the parabola and deviation of the corrugated pipe influence on radial force were discussed. Finally, conclusions and suggestion for future design and analysis are provided on the basis of the proposed investigation.

FIELD OBSERVATION OF BOTTOM PLATE FAILURE

Background information of Linguo bridge

The field observation of bottom plate failure is from the Linguo Bridge. The Linguo Bridge is a long-span continuous rigid frame bridge across the Gunong River with a main span of 180 m and two side spans of 85 m (Figure 1).

The width of the top plate of a single box cross section is 12.1 m, and its bottom and flange plates are 7 and 2.55 m wide, respectively. The height of the cross section is 3.5 m at the centre of the middle span and the support position of the side span. The position of the pier top is 11.5 m, and the height from the position of the pier top to the centre of the middle span or the support position of the side span is varied as 1.8 times parabola. The thickness of the bottom plate is 0.3 m at the centre of the middle span and the support position of the side span, which is at 1.3 m at the position of the pier top. Three kinds of thicknesses are distributed for the web, that is, 0.7, 0.6 and 0.5 m from the position of the pier top to the centre of the middle span or the support position of the side span. Up to 18 prestressed corrugated pipes are distributed at the bottom plate near the closure segment (Figure 1a and b). Each pipe consists of 19 prestressed strands, which consist of 9 high-strength galvanised steel wires.

Failure of bottom plate

The Linguo Bridge was constructed by adopting the cast-in-

(a) Longitudinal cracks along the span direction

(b) Crushed zone on the bottom plate

Figure 2: Cracks and crushed zone distributed on the bottom plate.

(a) Collapse of the bottom plate

(b) Concrete in the collapse region

Figure 3: Collapse of the bottom plate.

place cantilever method, which is a traditional and reliable method. Two closure segments were installed at the side span and one for the middle span (Figure 1). Closure construction was first performed at the side spans and then in the middle span. In May 15, 2015, the closure segment of the middle span was constructed, which indicated the closure of the Linguo Bridge. After 7 days, the prestressed strands were crossed and tensioned with the testing of the closure segment concrete strength, which satisfied the design standards, and cement grout was applied. The whole process of closure construction was successful according to the design standards. On May 23, 2015, failure was found on the bottom plate. One region was at a range of 4.65 to 5.53 m at the left side of the closure segment. The other region was at a range of 4.75 to 5.80 m at the right side of the closure segment. The most severe failures were located between segments No. 21 and 22, as well as No. 24 and 25 (Figure 1a). Careful investigation showed three typical problems on the bottom plate, namely, the longitudinal cracks and crushed zones, splitting of the bottom plate, and the deflection and deformation of the prestressed corrugated pipe (Figures 2 to 4).

The main crack was longitudinal along the span direction (Figure 2). Many crushed zones on the bottom plate were distributed along the main crack. Additionally, irregular form of waterlogging was formed. Large amount of concrete was lost when hammered slightly.

Figure 3 shows that the concrete of the bottom plate was damaged, and the concrete cover was peeled off from the bottom plate at the connection of the web and the bottom plate. The covered concrete was removed, and the distribution and connection of the reinforcing bar in the concrete were explored. In this region, the concrete and reinforcing bar were separated, and no bond was found between the transversal and longitudinal reinforcing bar. In addition, no bond was detected at the connection of the longitudinal reinforcing bar.

Figure 4 shows that the bottom plate was deformed and the large deformation in the reinforced concrete was always accompanied with cracking. Corrugated pipes were found to be deflected significantly (Figure 4b). The bottom plate was split by the huge prestressed action.

SIMPLIFIED MECHANICAL EXPLANATION OF DIFFERENT TYPES OF FAILURE

Simplified mechanism explanation

Figures 2 to 4 show the three typical destruction

(a) Deformation of the reinforcing bar **(b)** Deflection of corrugated pipe

Figure 4: Deflection and deformation of the bottom plate.

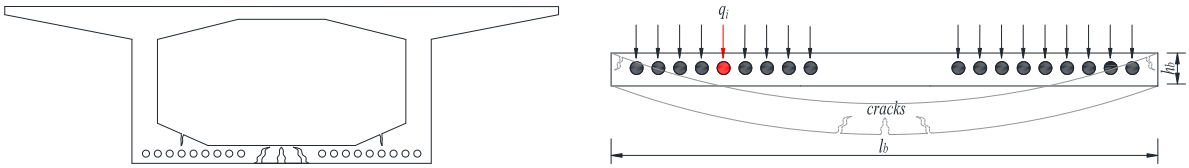

(a) Longitudinal cracks of bottom plate **(b)** Mechanism model of lateral deflection

Figure 5: Longitudinal cracking and mechanism model of the bottom plate.

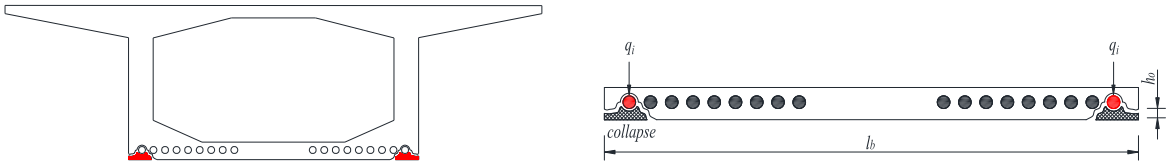

(a) Partial collapse of bottom plate **(b).** Mechanism model of punching shear failure

Figure 6: Partial collapse and mechanism model of the bottom plate.

characteristics for the failure of the bottom plate: bending crack; splitting and punching shear failure; failure due to radial load caused by prestressing.

Bending crack failure of bottom plate

As shown in Figure 2, longitudinal cracks in the box girder with wide bottom plate were evident. The transverse deflection of the bottom plate was analysed as the horizontal frame structure under the radial uniform load, and the bottom can be simplified as a beam with both ends fixed, as shown Figure 5b.

The bottom plate, indicated in Figure 5b, is simplified as a consolidation beam at both ends. With the action of the radial force, positive bending moment occurred at middle of the beam, and negative bending moment occurred at both fixed ends, as shown in Figure 5b. For the thickness of the bottom plate, h_b is only 0.28 m, the resistance rigidity for the bending moment per unit length is low. When the accumulative total of the bending moment excess the limitation, the cracks will be generated, and the cracking failure will be found, as shown in Figure 5.

Punching shear failure of bottom plate

As indicated in Figure 3, the concrete located at the corner of the box section was collapsed, where the thickness of the concrete cover was thin, and the reinforcing bar was not present. Under the action of the prestressed strand, the mechanism model of punching shear failure can be simplified as shown in Figure 6b.

From Figure 6b, it can be found that the punching shear failure was induced by the radial uniform load of the curved or broken prestressed strands. The punching shear stress for the shadow region concrete was mainly induced by the upper prestressed strand, which depends on the radial

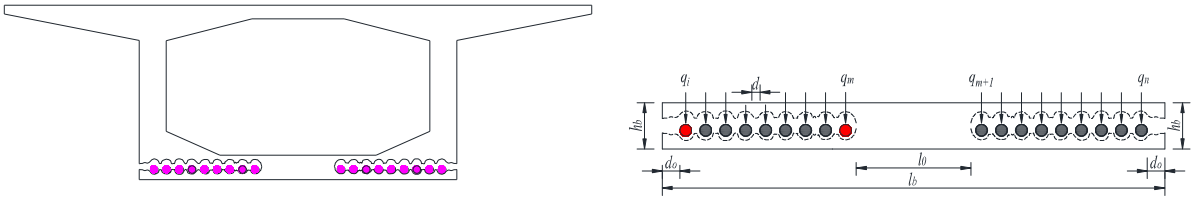

(a) Splitting of bottom plate **(b)** Mechanism model of splitting

Figure 7: Splitting and mechanism model of the bottom plate.

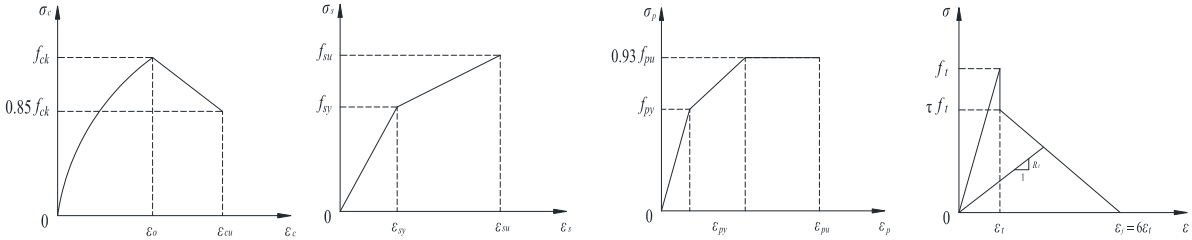

(a) Concrete (b) Steel bar (c) Prestressed strand (d) Concrete softening model

Figure 8: Material and structural failure model.

force, the effective height of the cone for punching shear and the circumference at the half height of the cone. If the induced punching shear stress is greater than the resistance strength of the bottom concrete, the punching shear failure would be found.

Splitting of bottom plate

The bottom plate indicated in this study shows that the cohesive strength was determined by the effect of the vertical reinforcing bar, axial tensile design strength and effective area of concrete. Figure 4 shows that effective vertical reinforcing bar was rarely found between the corrugated pipes. Additionally, the effective area for resistance tension was found to be very limited because the corrugated pipes occupied large areas (Figure 7). The bottom plate was split into upper and lower layers under the radial load caused by the prestressing.

Failure analysis of FE method

The above mechanism explanation only provides a qualitative description for the possible failure reasons. The development of a model to simulate the behaviour of prestressed concrete structures should consider the accurate modelling of the biaxial stress–strain behaviour of the concrete, steel bar and prestressed strands to understand the structural behaviour and failure mechanism of the system. Detailed finite element simulation can help the mechanism understanding and failure prediction of structures (Hognestad et al., 1955; Al-Manaseer and Phillips, 1987; Foster et al., 1996; Alwathaf et al., 2011) and is pursued here.

Material models

Linear isotropic and multilinear isotropic material properties are required to properly model concrete and prestressed strands to conduct nonlinear analysis of the failure process. As proposed by Hognestad et al. (1955), the multilinear isotropic material used the Von Mises failure criterion along with the Willam and Wamke model to define the failure of the concrete (Xiang et al., 2010). The applicable code JTG D62-2004 was also applied (Wu and Gilbert, 2009). The strain–stress curve is shown in Figure 8a and the relationship of stress and strain can be written as follows:

$$\begin{cases} \sigma_c = f_{ck}\left[2\left(\dfrac{\varepsilon_c}{\varepsilon_0}\right)-\left(\dfrac{\varepsilon_c}{\varepsilon_0}\right)^2\right] & 0 \le \varepsilon_c \le \varepsilon_0 \\ \sigma_c = f_{ck}\left[1-0.15\left(\dfrac{\varepsilon_c-\varepsilon_0}{\varepsilon_{cu}-\varepsilon_0}\right)\right] & \varepsilon_0 < \varepsilon_c < \varepsilon_{cu} \end{cases} \quad (1)$$

where f_{ck} is the uniaxial compressive strength of concrete. ε_{cu} is the ultimate compression strain and ε_0 is the strain at

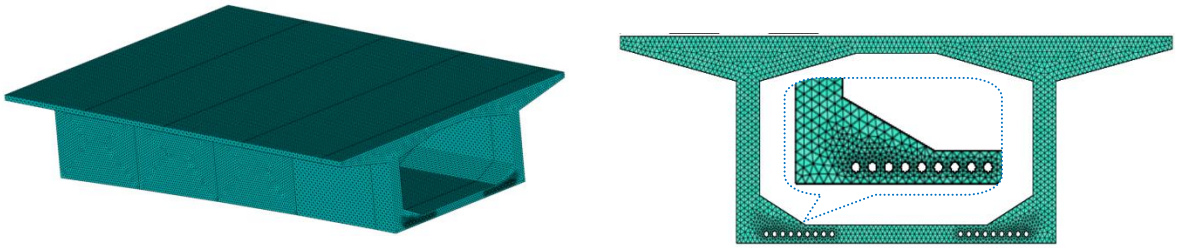

(a) Outlay of FE model

(b) Detail of the cross-section in FE model

Figure 9: 3D FE Model of Linguo Bridge.

the peak stress, which can be computed according to $\varepsilon_0 = 2f_c/E_0$, with E_0 as the initial tangent modulus.

Figure 8b shows the uniaxial stress–strain model for the steel bar for the current analysis. The model is a bilinear model. The relation is linearly elastic up to the steel yield stress (f_{sy}) followed by linear hardening up to the steel ultimate strength (f_{su}), which can be expressed as follows:

$$\begin{cases} \sigma_s = f_{sy}\dfrac{\varepsilon_s}{\varepsilon_{sy}} & 0 \le \varepsilon_s \le \varepsilon_{sy} \\ \sigma_s = \left(f_{su} - f_{sy}\right)\left(\dfrac{\varepsilon_s - \varepsilon_{sy}}{\varepsilon_{su} - \varepsilon_{sy}}\right) + f_{sy} & \varepsilon_{sy} < \varepsilon_s \le \varepsilon_{su} \end{cases} \quad (2)$$

where f_{sy} is the steel yield stress, f_{su} is the steel ultimate strength and ε_{sy} is the yield strain. E_s is the initial steel modulus, which can be obtained according to $E_s = f_{sy}/\varepsilon_{sy}$; ε_{su} is the ultimate strain, and E_{sh} is the strain hardening modulus, which can be obtained according to $E_{sh} = (f_{su} - f_{sy})/(\varepsilon_{su} - \varepsilon_{sy})$.

A typical tri-linear model of the prestressed strands is considered as the uniaxial stress–strain model for analysis (Figure 8c). The relation of the stress–strain of the prestressed strands can be expressed as follows:

$$\begin{cases} \sigma_p = f_{py}\dfrac{\varepsilon_p}{\varepsilon_{sy}} & 0 \le \varepsilon_p \le \varepsilon_{sy} \\ \sigma_p = f_{py} + \dfrac{0.09 f_{pu}}{0.015 - \varepsilon_{sy}}(\varepsilon_p - \varepsilon_{sy}) & \varepsilon_{sy} < \varepsilon_p \le 0.015 \\ \sigma_p = 0.93 f_{pu} & \varepsilon_p > 0.015 \end{cases} \quad (3)$$

where f_{py} is the steel yield stress, f_{pu} is the steel ultimate strength, ε_{py} is the yield strain and ε_{pu} is the ultimate strain.

Figure 8d shows that the smeared crack concept was adopted in the proposed analysis. The orientation of cracks in the model was determined by the direction of the principal stress when the crack initiation criterion was met (Al-Manaseer and Phillips, 1987; Foster et al., 1996; Alwathaf et al., 2011). The material was then treated as an orthotropic material with orthotropic axes fixed with the directions of initial principal stresses. f_t is the tensile strength of the concrete. ε_t is the corresponding tensile strain. ε_f is the maximum tensile strain, which can be calculated according to $\varepsilon_f = 6\varepsilon_t$. R_t is the softening of the secant modulus, and τ is the material parameter.

3D FE model

One of the nine-segment beam was selected as the study case to examine the splitting of the bottom plate. A 3D FE model, consisting of 201,346 nodes and 907,197 elements, was built using the ANSYS program for half of the nine-segment beam (Figure 9). The SOLID65 element, with eight nodes and three degrees of freedom at each node, was used to model the concrete, which can simulate the plastic deformation and cracking in the three orthogonal directions. LINK10 element was used for prestressed strands. The concrete and the prestressed strands were connected through the coupling of the common nodes. The prestressed loading was simulated and realized by the temperature decrease of the LINK10 element. The boundary conditions at the left section of the FE model were fixed along the *x*, *y*, and *z* directions.

Results of FE analysis

Calculation was conducted using the FE model (Figure 9). The stress of the bottom plate induced by the prestressed effect was obtained (Figures 10 to 13). Due to space limitation, only one segment's calculation result was choice to analysis.

The maximum stress in *x* direction for the bottom plate was concentrated on the chamfer of bottom plate and web plate (Figures 5 and 10). The maximum value of this stress, combined with the action of the radial force of prestressed strands, was found to be as high as 3.81 MPa. The maximum tension at the bottom edge of the bottom plate was distributed at the central and the value reached 3.12 MPa.

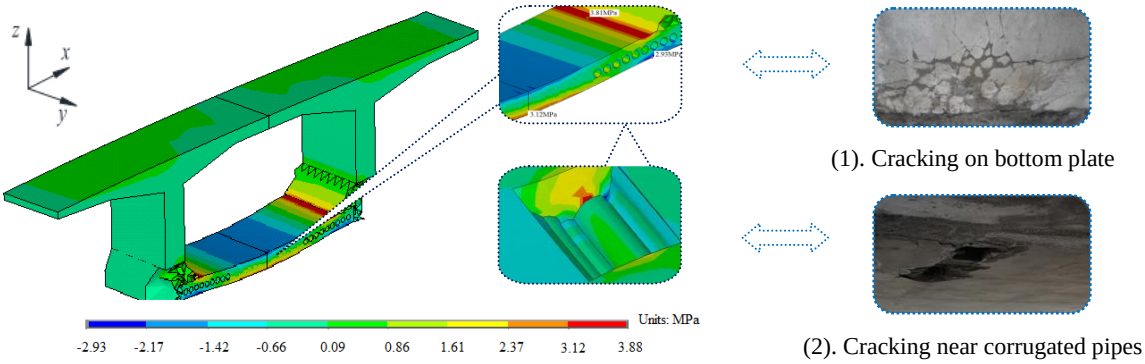

(a). Calculated stress of bottom plate in *x* direction **(b)**. Field test

Figure 10: Calculated stress and field test failure of the bottom plate in *x* direction.

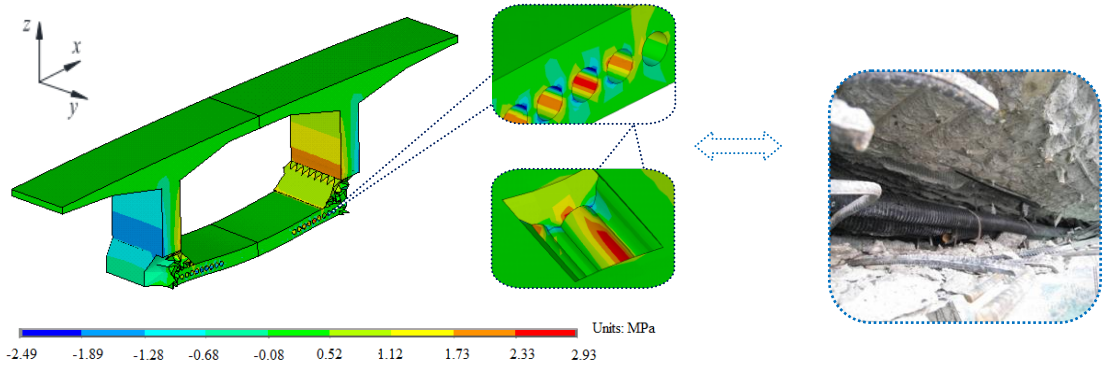

(a). Calculated Shear stress of bottom plate **(b)**. Field test

Figure 11: Calculated shear stress and field test failure of the bottom plate.

The maximum values of tensile stress for the bottom plate are greater than the resistance stress 2.85 MPa. A comparison of Figure 10a and b shows that the distribution of the calculated tensile stress agrees with field observation failures.

Figure 11a shows that shear stress varied from −2.49 to 2.93 MPa, with the maximum value at the bottom plate distributed around the corrugated pipes. The shear strength was 2.52 MPa according to the design code JTG D62–2004. Obviously, a punching shear failure occurred, which was also observed at the corner of the box section, as shown in Figure 11b. A further comparison of Figure 11a and b shows that the calculated results are in agreement with the field observations for the punching shear failure mechanism (Figure 6).

Figure 12a shows that the maximum compressive stress was distributed at the top of the bottom plate, and the value was as high as 13.80 MPa. The compressive stress of the concrete adjacent to the corrugated pipes caused by the reduced compressed area reached 13.20 MPa, and the minimum value was 11.90 MPa. Figure 10 and 11 show that the concrete adjacent to corrugated pipes experienced cracking and punching shear failure caused by the prestressed strands, and the bottom plate would be split into upper and lower layers along the positions of the longitudinal corrugated pipes. In addition, under the action of the longitudinal (in *y* direction) stress, the splitting bottom plate would show buckling instability, and extreme displacement and deformation often occurred together (Figure 12b). Furthermore, the concrete split in the lower layer of the bottom plate along the longitudinal prestressed strands would be crushed (Figure 2b).

REINFORCEMENT PROCEDURE AND RESULTS

The bottom plate failure shows that the Linguo Bridge should be reinforced to ensure the safety of the structure. Reinforcement should be performed such that the function and the durability of the structure meet the design requirements. Two methods can be used to reinforce such structural deficiencies, namely, reinforcement with bonding steel plate and reinforcement with transverse rib. The former method is easier to construct than the latter one. In

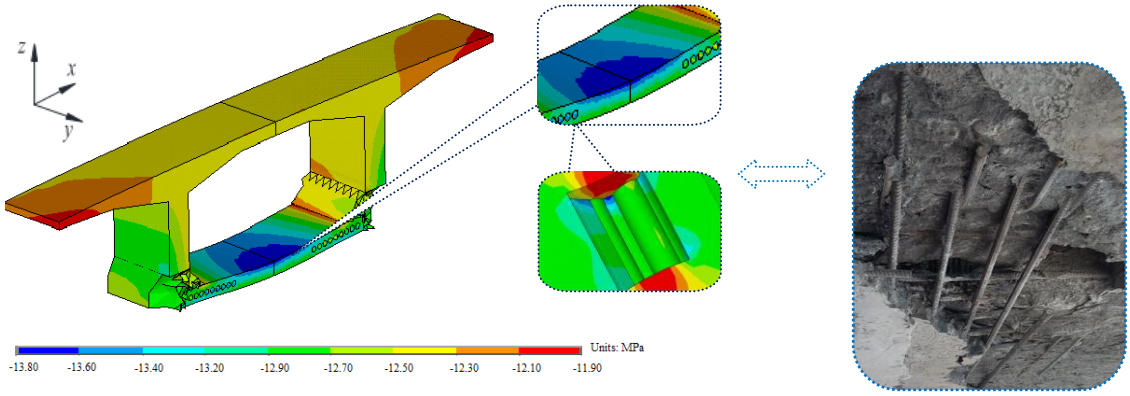

(a). Calculated stress of bottom plate in *y* direction **(b)**. Field test

Figure 12: Calculated stress and field test failure of bottom plate in *y* direction.

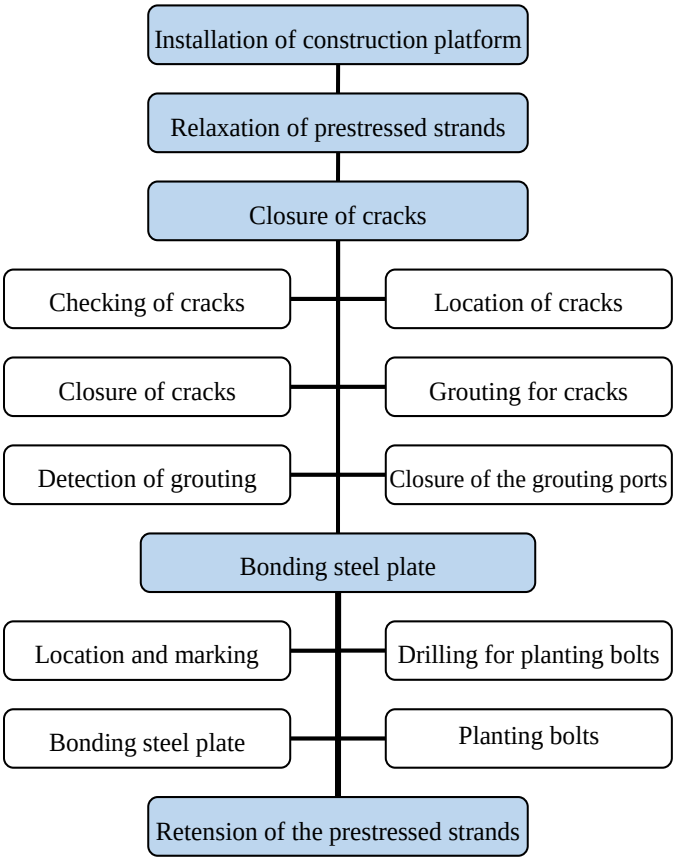

Figure 13: Procedure of reinforcement.

addition, in comparison of the reinforcement with bonding steel plate, reinforcement with transverse rib has heavier weight of concrete when the transverse rib is larger. Thus, bonding steel plate is considered during the reinforcement for Linguo Bridge.

Procedure of bonding steel plate

The deficiency shown in Figures 2 to 4 shows that the cracks would be closed, fractural steel bars would be welded and the concrete of punching shear and splitting failure would be reinforced. The reinforcement process is presented in Figure 13.

Figure 13 shows the seven basic steps applying the reinforcement of bonding steel plate as follows: relaxation of prestressed strands, closure of cracks, planting of bolts, bonding steel plate, repairing of bottom plate concrete and retension of the prestressed strands. The relaxation of the prestressed strands was symmetrically schemed from BP9 to BP1, as shown in Figure 14.

The cracks distributed on the bottom plate should be closed to meet the durability of the concrete structure. In this phase, the number, length and distribution of the cracks were investigated, which are important references for the scheme of grouting. The cracks should be cleansed and dried prior to grouting. Single grouting or multi-grouting depends on the size and region of the crack. Grouting pressure is set to be 0.2 MPa.

The bonding of steel plate is one of the most important steps during reinforcement. This step includes the location, marking and drilling for panting bolts to prepare the bonding of the steel plate. The location for drilling should be accurate, and the destruction of the prestressed corrugated pipe should be avoided. The final step involved the retension of the prestressed strands. The process and tension grade should be strictly decided in accordance with the requirements of the design. The deformation and stress of the beam should also be monitored.

Stress monitoring during reinfocement

Six stress sensors were installed at different locations on

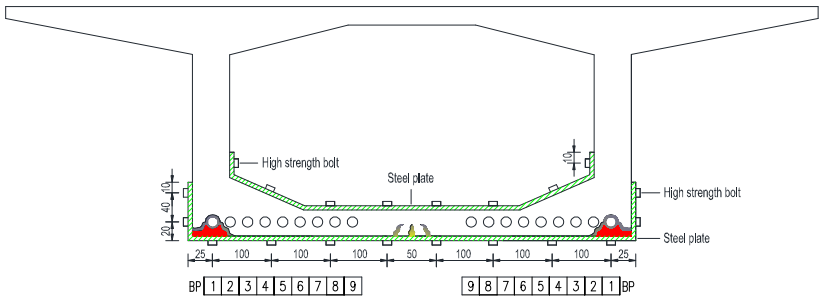

Figure 14: Reinforcement with bonding steel plate.

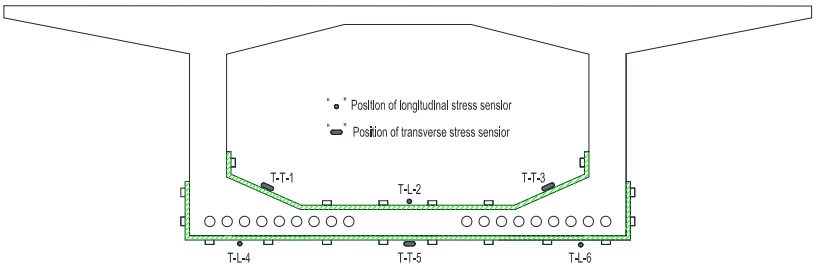

Figure 15: Arrangement of stress sensors.

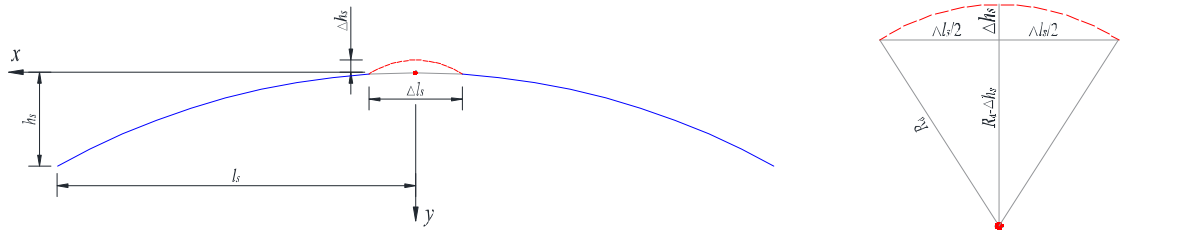

(a) Dimension of the parabola

(b) Deviation of the corrugated pipe

Figure 16: Geometry of the prestressed strand curve.

the bottom plate of the closure segment to collect stress data during construction and thus monitor the deformation and stress of the bottom plate of the box beam. The positions of the stress sensors in the middle of the closure segment for the Linguo Bridge are plotted in Figure 16. T-T-1, T-T-3 and T-T-5 were transverse stress sensors, which were mounted to monitor transverse stress. T-L-2, T-L-4 and T-L-6 were the longitudinal stress sensors, which were mounted to monitor longitudinal stress.

Real-time stress were monitored and the characteristics of stress variation during construction were investigated. Two typical construction stages had relatively high stress, that is, retension of prestressed strands and application of secondary dead load. The measured results are shown in Table 1 together with the calculation results using the proposed finite element method.

Table 1 shows that the stress of the bottom plate did not vary remarkably. No new cracks were found and old cracks did not develop during reinforcement. These findings demonstrate the effectiveness of the reinforcement process. Table 1 also shows that the transverse tensile stress of concrete bottom plate during the construction of secondary dead load slightly increased as compared with that of the construction of prestressed strand retension, while the longitudinal compression stress slightly decreased. The calculated results of the stress and field tests showed that the variations of stress ranged from 10.4 to 15.5%. The magnitude of the calculated stress is on the conservative side as compared with the field measurements.

DISCUSSION

Analytical results showed that the radial force is the most direct and most critical factor for the splitting of the bottom plate. The height of the cross section for the beam in the

Table 1 Stress comparison of construction stages.

Items	Construction of prestressed strand retension						Construction of secondary dead load					
	T-T-1	T-L-2	T-T-3	T-L-4	T-T-5	T-L-6	T-T-1	T-L-2	T-T-3	T-L-4	T-T-5	T-L-6
Calculated stress (MPa)	2.38	−12.80	2.38	−10.61	3.10	−10.60	2.54	−13.71	2.54	−11.71	3.36	−11.71
Field test stress (MPa)	2.02	−10.82	2.09	−9.20	2.72	−9.41	2.21	−12.11	2.16	−10.22	3.01	−10.12
Variations (%)	15.1%	15.5%	12.2%	13.3%	12.3%	11.2%	13.0%	11.7%	15.0%	12.7%	10.4%	13.6%

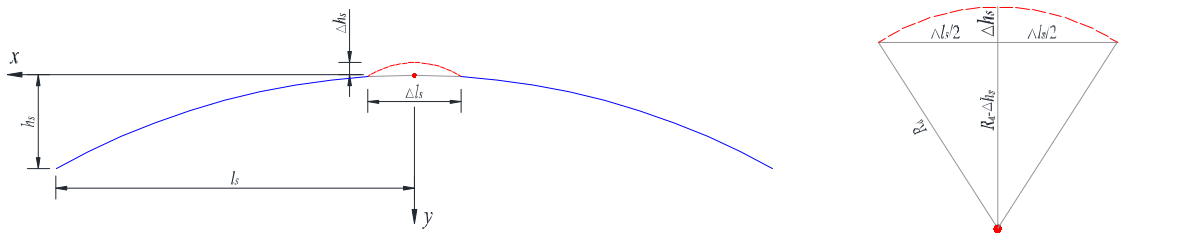

(a) Dimension of the parabola **(b)** Deviation of the corrugated pipe

Figure 16: Geometry of the prestressed strand curve.

majority of the continuous box girder bridge, as well as the prestressed strands, varied as a parabola. The indices of the parabola and deviation of the corrugated pipe were found to be the important factors of the radial force. The influence of radial force with systematic parametric studies should be investigated to further understand the influence factors of the radial force.

Radial uniform load is generated and applied on the bottom plate because of the curvature, with the action of the prestressed strand. The load may be expressed as:

$$q = \frac{F}{R} \tag{4}$$

where q is the radial uniform load, F is the force of the prestressed strand and R is the radius of the curvature. The radial uniform load was the main cause of the splitting of the bottom plate, which was induced by the curvature of the prestressed strand and the positional deviation of the corrugated pipe during construction (Figure 16).

The equation for the strand may be derived as follows according to the parabola shown in Figure 16a:

$$y = \frac{h_s}{l_s^k} x^k \tag{5}$$

where k is the index of parabola, h_s is the height of the parabola and l_s is the half projection length of the prestressed strand in the x direction.

The first-order derivative of Equation (5) with respect to the variable x is calculated as follows:

$$y' = k\frac{h_s}{l_s^k} x^{k-1} \tag{6}$$

The derivative of Equation (6) with respect to variable x is calculated as follows:

$$y'' = k(k-1)\frac{h_s}{l_s^k} x^{k-2} \tag{7}$$

The radius of the curvature can be obtained by combining Equations (6) and (7) as follows:

$$R_p = \frac{(1+y'^2)^{1.5}}{|y''|} \tag{8}$$

where R_p is the radius of the curvature for the parabola.

Substituting Equation (8) into Equation (4) will result in the following equation:

$$q_p = F\frac{|y''|}{(1+y'^2)^{1.5}} \tag{9}$$

where q_p is the radial uniform load induced by the prestressed strand of the parabola.

The positional deviation of the corrugated pipe is shown in Figure 16(b). The length of the deviation curve was shorter than that of the parabola, which can be considered as a short circular arc. The radius of the deviation curve can be expressed as follows:

$$R_d = \frac{\Delta l_s^2}{8\Delta h_s} + \frac{\Delta h_s}{2} \tag{10}$$

where R_d is the radius of the curvature for the deviation curve, Δl_s is the chord length of the deviation curve and Δh_s

Table 2: Deviation of the corrugated pipe influence on radial force.

Spacing between the location of steel bars Δl_s (m)	Deviation of the corrugated pipe Δh_s (m)	Radius R_d (m)	Tension of strands F (kN)	Radial force q_d (kN/m)
1000.0	2.0	62.50	4452.84	71.24
1000.0	4.0	31.25	4452.84	142.48
1000.0	6.0	20.84	4452.84	213.71
1000.0	8.0	15.63	4452.84	284.91
1000.0	10.0	12.51	4452.84	356.08
1000.0	12.0	10.42	4452.84	427.23
1000.0	14.0	8.94	4452.84	498.33
1000.0	16.0	7.82	4452.84	569.38
1000.0	18.0	6.95	4452.84	640.38
1000.0	20.0	6.26	4452.84	711.32

is the distance between the apices of the parabola and the deviation curve.

Substituting Equation (10) into Equation (4) will yield the following equation:

$$q_d = \frac{8F\Delta h_s}{\Delta l_s^2 + 4\Delta h_s^2} \tag{11}$$

where q_d is the radial uniform load induced by the prestressed strand of the deviation curve.

Combination of Equations (9) and (11), the radial force can be expressed as follows:

$$\begin{aligned} q &= q_p + q_d \\ &= \frac{F|y''|}{(1+y'^2)^{1.5}} + \frac{8F\Delta h_s}{\Delta l_s^2 + 4\Delta h_s^2} \end{aligned} \tag{12}$$

Index of parabola influence on radial force

Four main spans, namely, 80, 160, 180 and 200 m, were considered cases to study the effects of the index of parabola. These spans are most typical and popular for continuous girder bridge and continuous rigid frame bridge. The indices of parabola k for the prestressed strands varied from 1.6 to 2.0, as shown in Table 2. The value of x was 4.00 m, which is a randomly studied position in the last segment of cantilever construction. The value of the tension of prestressed strands F was 4452.84 kN, which was the tension of 19 prestressed strands with a radius of 15.24 mm. The radius of the curve strands and the radial force can be calculated using Equation (9), and the results are shown in Table 3.

The radius and radial forces are shown in Table 2 to further investigate the relationships among the indices of parabola. Variation curves of the effect of the index of parabola on radius and radial force are shown in Figures 17 and 18.

Table 2 shows that the radial force q_p varied from 27.32 to 24.52 kN/m with indices from 1.6 to 2.0 for the main span of 80.0 m. In contrast, radial forces varied from 17.40 to 11.48 kN/m, 16.06 to 9.86 kN/m and 14.89 to 8.92 kN/m for spans of 160, 180 and 200 m, respectively. Thus, radial force decreased with increasing index of the parabola. Meanwhile, longer main span indicates lower radial force. Thus, radial force decreased with increasing main span, as shown by the main spans of 80 and 200 m. The radial force of the former was obviously higher than that of the latter.

Therefore, a high index of parabola should be adopted with the permission of the structural dimension during the design phase. In addition, too much prestressed strands, such as those with relatively shorter span at 80 m, should be avoided to reduce the influence of the radial force.

Influence of deviation of corrugated pipe on radial force

Deviation of prestressed corrugated pipe positioning is inevitable during construction, particularly at the connection position between the adjacent segments. This deviation changes the space position of the prestressed steel strands, affecting the radial force. The spacing between the positions of the steel bars for the prestressed corrugated pipe is usually 1000 mm.

The deviation of the corrugated pipe varied from 2 to 20 mm, and the radial force induced by the different deviations of the corrugated pipe was obtained using Equation (11) (Table 2).

The relationships between the deviation of the corrugated pipe, radius and radial force, combined with the data shown in Table 3, were investigated. Variation curves of the radius and radial force affected by the deviation of the corrugated pipe are shown in Figures 19 and 20.

Table 3: Comparison of indices of parabola influence.

Main span (m)	l_s (m)	h_s (m)	Index of parabola k	Calculated Position x (m)	Radius R_p (m)	Tension of strands F (kN)	Radial force q_p (kN/m)
	33.00	3.00	1.60	4.00	162.99	4452.84	27.32
	33.00	3.00	1.70	4.00	162.27	4452.84	27.44
80.00	33.00	3.00	1.80	4.00	165.52	4452.84	26.90
	33.00	3.00	1.90	4.00	172.07	4452.84	25.88
	33.00	3.00	2.00	4.00	181.63	4452.84	24.52
	71.00	6.50	1.60	4.00	255.91	4452.84	17.40
	71.00	6.50	1.70	4.00	275.16	4452.84	16.18
160.00	71.00	6.50	1.80	4.00	303.09	4452.84	14.69
	71.00	6.50	1.90	4.00	340.25	4452.84	13.09
	71.00	6.50	2.00	4.00	387.83	4452.84	11.48
	85.00	8.00	1.60	4.00	277.27	4452.84	16.06
	85.00	8.00	1.70	4.00	303.55	4452.84	14.67
180.00	85.00	8.00	1.80	4.00	340.45	4452.84	13.08
	85.00	8.00	1.90	4.00	389.14	4452.84	11.44
	85.00	8.00	2.00	4.00	451.62	4452.84	9.86
	90.50	8.20	1.60	4.00	299.02	4452.84	14.89
	90.50	8.20	1.70	4.00	329.42	4452.84	13.52
200.00	90.50	8.20	1.80	4.00	371.81	4452.84	11.98
	90.50	8.20	1.90	4.00	427.66	4452.84	10.41
	90.50	8.20	2.00	4.00	499.45	4452.84	8.92

Results shown in Table 3 and Figures 19 and 20 indicate that the radii decreased from 62.50 to 6.26 m, and the radial force increased from 71.24 to 711.32 kN/m with the increase in deviation of the corrugated pipe from 2.0 to 20.00 mm. Thus, higher deviation will result in smaller radius but with larger radial force. The deviation and radial force showed a nearly linear relationship, as compared with the negative relationship of deviation of the corrugated pipe with the radius.

Tables 2 and 3 show that the largest radial force q_p induced by the index of the prestressed strands parabola was 27.32 kN/m, while the least value of the radial force q_d induced by the deviation of the corrugated pipe was 71.24 kN/m. Thus, the former is far less than the latter. Furthermore, the influence of the deviation of the corrugated pipe is much greater than that of the index of the prestressed strand parabola. Therefore, the deviation of the corrugated pipe is not only highly sensitive but is also the main influencing factor of the radial force.

Conclusions

Failure mechanism and reinforcement of bottom plate for box girder bridge during prestressing were investigated using field testing and 3D FE simulation framework. The following conclusions were drawn:

1). Refined nonlinear 3D FE model is shown to successfully represent the mechanical reason for the three failure modes identified from field testing: bending cracking, punching shear failure, and splitting of bottom plate coupled with crushing of the concrete;.

2). The radial force is important for the observed bottom plate failure although such force is not considered in existing codes. A high index of the parabola of the prestressed strand should be adopted as far as possible to decrease the radial force. Moreover, the steel bars should be arranged to avoid the punching shear failure and splitting of the bottom plate.

3). The deviation of the prestressed corrugated pipe during the construction is critical for the splitting failure. During prestressing, spacing should be shortened, and the number of positioning of steel bars should be increased to directly decrease the deviation of the prestressed corrugated pipe.

4). With the proposed bonding steel plate reinforcement, the longitudinal cracks were effectively closed, the splitting bottom plate was bonded and local punching shear damage was also repaired. The bearing capacity of the structure was restored, and the appearance of the structure was also very clean and tidy. Therefore, the proposed method is an effective and direct way to model failures and similar ones

in project fields.

The proposed study focuses on the construction stage with only prestressing load. Further investigation with both numerical simulation and field observations on the long term durability of bottom plate, including cyclic vehicle load and environmental corrosion effects should be done. In addition, systematic health monitoring and damage diagnosis for the bridge bottom plate using advanced sensing technology should be developed for the accurate state awareness of damage initiation and propagations under service operations.

ACKNOWLEDGEMENTS

The research described in this study was financially supported by the National Basic Research Program of China (973 Program, 2015CB057701), the Natural Science Foundation of China (51308071, 51378081), the Natural Science Foundation of Hunan Province (13JJ4057), the Foundation of China Scholarship Council (201408430155), and the Traffic Department of Applied Basic Research Project (2015319825120).

REFERENCES

Barr PJ, Stanton JF, Eberhard MO (2005). Effects of temperature variations on precast, prestressed concrete bridge girders. J. Bridge Eng. 10(2): 186-194.

Moon D Y, Sim J, Oh H. Practical crack control during the construction of precast segmental box girder bridges. Comput. Struct. 2005; 83(31): 2584-2593.

Pan Z, Fu C C, Jiang Y. Uncertainty analysis of creep and shrinkage effects in long-span continuous rigid frame of Sutong Bridge. J. Bridge Eng. 2010; 16(2): 248-258.

Jung K H, Yi J W, Kim J H J. Structural safety and serviceability evaluations of prestressed concrete hybrid bridge girders with corrugated or steel truss web members. Eng. Struct. 2010; 32(12): 3866-3878.

Malm R, Sundquist H. Time-dependent analyses of segmentally constructed balanced cantilever bridges. Eng. Struct. 2010; 32(4): 1038-1045.

Xiang Y, Tang G, Liu C. Cracking mechanism and simplified design method for bottom flange in prestressed concrete box girder bridge. J. Bridge Eng. 2010; 16(2): 267-274.

Xu Y, Liang L, Song S. Repairing Method and Finite Element Simulation Analysis of Bottom Slab with Bursting Cracks of a Continuous Rigid-Frame Bridge. Bridge Constr. 2007; 4: 70-74.

Peng Y C. Cause Analysis and Countermeasures for Bursting Cracks in Box Girder Bottom Slabs of Continuous Rigid-Frame Bridges. Bridge Constr. 2008; 3: 67-70.

El-Ariss B. Behavior of beams with dowel action. Eng. Struct. 2007; 29(6): 899-903.

Bazant Z P, Li G H, Yu Q, Klein G, Kristek V. Explanation of excessive long-time deflections of collapsed record-span box girder bridge in Palau. Proc., 8th Int. Conf. on Creep, Shrinkage and Durability of Concrete and Concrete Structures. The Maeda Engineering Foundation, Ise-Shima, Japan, 2008: 1-31.

Podolny W J. The cause of cracking in post tensioned concrete box girder bridges and retrofit procedures. PCI J. 1985; 30(2): 82–139.

Podolny W J. The cause of cracking in post tensioned concrete box girder bridges and retrofit procedures. PCI J. 1985; 30(2): 82–139.

Wei L, Sheng X, Xiao R. Mechanism and prevention countermeasures of cracking for bottom slab in a continuous prestressed concrete box girder. Struct. Eng. 2007; 23(2): 53–57.

Pan D, Zhao Q, Wang J. Mechanism of breaking in bottom slab of prestressed reinforced concrete continuous box girder. J. PLA Univ. Sci. Technol. (Nat. Sci. Ed.) 2008; 9(5): 552–556.

Megally S, Seible F, Garg M, et al. Seismic performance of precast segmental bridge superstructures with internally bonded prestressing tendons. PCI J. 2002; 47(2): 40-56.

Liao J, Ye G, Xu X. Analysis of cracks in continual box-girder with prestressed concrete bridge and assessment of reinforcement. China J Highway Trans., 2004, 17(1): 62-65.

Sennah K M, Kennedy J B. State-of-the-art in design of curved box-girder bridges. J. Bridge Eng. 2001; 6(3): 159-167.

Ataei N, Padgett J E. Limit state capacities for global performance assessment of bridges exposed to hurricane surge and wave. Struct. Saf. 2013; 41: 73-81.

AASHTO, LRFD. AASHTO LRFD bridge design specifications. AASHTO, Washington, D.C. 2007.

JTG D62-2004. Design Code for Design of Highway Reinforced Concrete and Pre-stressed Concrete Bridge Culvert. 2004.

Bergan P G, Holand I. Nonlinear finite element analysis of concrete structures. Comput. Meth. Appl. Mech. Eng. 1979; 17: 443-467.

Orta L, Bartlett F M. Reliability analysis of concrete deck overlays. Struct. Saf. 2015; 56: 30-38.

Sousa H, Bento J, Figueiras J. Construction assessment and long-term prediction of prestressed concrete bridges based on monitoring data. Eng. Struct. 2013; 52: 26-37.

Wu H Q, Gilbert R I. Modeling short-term tension stiffening in reinforced concrete prisms using a continuum-based finite element model. Eng. Struct. 2009; 31(10): 2380-2391.

Zhou S J. Finite beam element considering shear-lag effect in box girder. J. Eng. Mech. 2010; 136(9): 1115-1122.

Lou T, Lopes S M R, Lopes A V. A finite element model to simulate long-term behavior of prestressed concrete girders. Finite Elem. Anal. Des. 2014; 81: 48-56.

Guo F, Qian Y, Li Z. Analysis of breaking of bottom slab in continuous prestressed concrete rigid frame bridge. J. Highway Transp. Res. Dev., 2005; 22(10): 68–70.

Pedziwiatr J. The influence of the bond between concrete and reinforcement on tension stiffening effect. Mag. Concrete Res. 2009; 61(6): 437-443.

Pimentel M, Figueiras J. Assessment of an existing fully prestressed box-girder bridge. Proceedings of the Institution of Civil Engineers-Bridge Engineering. Thomas Telford Ltd 2015; 1-12.

Chen L, Tang G B. Influence of Longitudinal Cracks in Bottom Flange of Concrete Continuous Box Girder. Appl. Mech. Mater. 2015; 744: 773-778.

Bathe K J, Walczak J, Welch A, Mistry N. Nonlinear analysis of concrete structures. Comput. Struct. 1989; 32(3): 563-590.

Tang X S, Zhang J R, Li C X, Xu F H, Pan J. Damage analysis and numerical simulation for failure process of a reinforced concrete arch structure. Comput. Struct. 2005; 83(31): 2609-2631.

Hognestad E, Honson N W, McHenry, D. Concrete stress distribution in ultimate strength design. ACI J. Proc., 1955; 52(6): 455–479.Al-Manaseer A A, Phillips D V. Numerical study of some post-cracking material parameters affecting nonlinear solutions in RC deep beams. Canadian J. Civ. Eng. 1987; 14(5): 655-666.

Foster S J, Budiono B, Gilbert R I. Rotating crack finite element model for reinforced concrete structures. Comput. Struct. 1996; 58(1): 43-50.

Alwathaf A H, Ali A, Jaafar M S, et al. Stress-strain modelling of reinforced concrete membrane structures. Int. J. Phys. Sci. 2011; 6(30): 6820-6828.